PAPER

Check for updates

Energetics and optical properties of carbon impurities in rutile TiO₂†

Supparat Charoenphon,[a] Adisak Boonchun,[ab] Daungruthai Jarukanont,[a] Jiraroj T-Thienprasert [iD] [ab] and Pakpoom Reunchan [iD] ⋆[ab]

Titanium dioxide is one of the most promising materials for many applications such as photovoltaics and photocatalysis. Non-metal doping of TiO₂ is widely used to improve the photoconversion efficiency by shifting the absorption edge from the UV to visible-light region. Here, we employ hybrid density-functional calculations to investigate the energetics and optical properties of carbon (C) impurities in rutile TiO₂. The predominant configurations of the C impurities are identified through the calculated formation energies under O-poor and O-rich growth conditions. Under the O-poor condition, we find that C occupying the oxygen site (C_O) is energetically favorable for Fermi-level values near the conduction band minimum (n-type TiO₂), and acts as a double acceptor. Under the O-rich condition, the C_i–V_{Ti} complex is energetically favorable, and is exclusively stable in the neutral charge state. We also find that interstitial hydrogen (H_i) can bind to C_O, forming a C_O–H_i complex. Our results suggest that C_O and C_O–H_i are a cause of visible-light absorption under oxygen deficient growth conditions.

1 Introduction

TiO₂ is a material of great interest in electronics and optoelectronics, especially in photocatalysis.[1] It is also a promising material for photovoltaic solar cells, especially for dye-sensitized solar cells.[2,3] TiO₂ exists as three polymorphs: rutile, anatase, and brookite. Both rutile and anatase TiO₂ have been extensively explored for photocatalytic applications and different photocatalytic activities have been reported for both polymorphs.[4,5] Besides, TiO₂ can be synthesized as coexisting polymorphs by various growth processes,[6,7] yielding better photocatalytic performance than that of an individual polymorph. In general, rutile TiO₂ has a large band gap of 3.0 eV (ref. 8 and 9) that can only be activated under UV light irradiation, a major drawback for photocatalysis applications. Therefore, it is of great interest to find ways to extend the absorption wavelength range of TiO₂ into the visible region without decreasing the photocatalytic activity. Various experimental techniques including dye sensitization[10,11] and transition metal doping[12–14] enable photocatalysts to operate under visible light irradiation. Recently, it has been reported that doping TiO₂ with non-metals

such as N, S or C extends the absorption edge from the UV to visible region.[15–17]

The intentional and controlled incorporation of C impurities into the TiO₂ lattice is an efficient method to enhance visible light photocatalytic activity.[18–26] Carbon-doped TiO₂ has been prepared using different synthetic methods[21,26] and the favorable configuration of carbon impurities in the TiO₂ lattice has been interpreted differently. In experiments, C dopants were often assumed to incorporate either as C substitutional on an O site (C_O)[18–21] or as C occupying an interstitial site (C_i).[22–25] In addition, the mechanism underlying visible-light absorption is still ambiguous.

First-principles calculations based on density-functional theory (DFT) have been established as an important tool for understanding and acquiring knowledge of the behavior of defects and impurities in materials. Valentin *et al.*[27] performed DFT calculations within the generalized gradient approximation (GGA)[28] to study various possible C doping species in both anatase and rutile TiO₂. In rutile, they found that carbon atoms energetically prefer to occupy an interstitial site next to an oxygen vacancy, C_i–V_O, under oxygen-poor conditions, whereas carbon atoms prefer to occupy the titanium site (C_{Ti}) under oxygen-rich conditions. Generally, standard DFT methods grossly underestimate band gaps. In their GGA calculations, the calculated band gap of rutile TiO₂ was 1.81 eV,[27] much lower than the experimental value, partly because of self-interaction errors in DFT.[29,30]

Most defects and impurities can introduce levels in the band gap, in which electrons can be exchanged with the Fermi-level. This causes impurities, including C in TiO₂ occurring in

*a*Department of Physics, Faculty of Science, Kasetsart University, Bangkok 10900, Thailand. E-mail: pakpoom.r@ku.ac.th

*b*Thailand Center of Excellence in Physics, Ministry of Higher Education, Science, Research and Innovation, 328 Si Ayutthaya Road, Bangkok 10400, Thailand

† Electronic supplementary information (ESI) available: (1) Chemical potential diagram for equilibrium growth of rutile TiO₂; (2) band structures and corresponding Brillouin zone; and (3) density of states of C_O. See DOI: 10.1039/d0ra02709j

multiple charge states. In their previous study, Valentin *et al.*[27] considered only the neutral charge state for all carbon impurities. Moreover, their calculated band gap of rutile TiO_2 was underestimated; this might lead to an incomplete conclusion.

In the present work, we investigate the energetics and optical properties of plausible C impurities in rutile TiO_2 in their stable charge states, including C_O, C_{Ti}, C_i, C_i–V_O and C_i–V_{Ti} complexes, through DFT calculations within the Heyd–Scuseria–Ernzerhof (HSE) hybrid functional for exchange and correlation. The HSE hybrid functional has been proven to yield not only a better description of the band gap, but also accurate defect levels and formation energies.[31,32] The energetically favorable configurations of carbon impurities for certain Fermi levels and growth conditions are determined based on formation energies. The optical transitions are estimated using configuration coordinate diagrams. We find that under the O-poor condition, C_O is energetically favorable in n-type TiO_2, where the Fermi-level position is near the conduction band. We find that the localized states above the valence band produced by C_O give rise to visible-light absorption. In addition, the effect of H impurities, which are ubiquitous and can unintentionally be incorporated in the material synthesis process, is considered. Our calculations indicate that interstitial H attracts C_O, forming a C_O–H_i complex. This complex could also be a cause of the visible-light absorption, unlike N_O–H_i, which eliminates the visible-light absorption effects of N_O in TiO_2.[33]

2 Computational method

Our DFT calculations were employed within the HSE hybrid-functional[34] and the projector-augmented wave (PAW) method[35] as implemented in the VASP code.[36] We used a well-converged energy cut-off of 420 eV for the projector-augmented plane waves. In this study, Ti $3s^2 3p^6 4s^2 3d^2$ states were treated as valence states. For the calculations of lattice parameters, band gaps, and formation enthalpies, we employed a 6-atom conventional unit cell with $5 \times 5 \times 7$ Monkhorst–Pack (MP) meshes for the Brillouin zone integrations.

In the HSE approach, the Coulombic potential in the exchange energy is divided into short-range and long-range parts with a screening length of 10 Å. In the short-range part, the non-local Hartree–Fock (HF) exchange is mixed with the Perdew, Burke and Ernzerhof (PBE) GGA exchange energy.[28] The long-range part and the correlation potential are represented by the PBE functional. We used the standard HF mixing $\alpha = 0.25$, which is suitable for satisfaction of the generalized Koopmans' theorem[37] in both anatase and rutile TiO_2.[38] Geometry relaxations were performed for the cell volume and shape, as well as for the atomic positions of the conventional cell until the residual force was less than 0.02 eV Å^{-1}.

For the calculations of C impurities, we extended the conventional cell by $2 \times 2 \times 3$ to produce a 72-atom supercell and introduced a defect in the supercell. For the Brillouin zone integrations of the supercell, the k-points were sampled at a non-Γ-centered MP $2 \times 2 \times 2$ mesh in which the Fock-exchange part[39] was reduced by a factor of 2. All atoms were allowed to relax with a fixed cell volume until the residual forces are less than 0.02 eV Å^{-1}.

The likelihood of incorporating an impurity in TiO_2 is determined by its formation energy, which depends on the O ($\tilde{\mu}_O$), Ti ($\tilde{\mu}_{Ti}$) and C ($\tilde{\mu}_C$) chemical potentials. For example, the formation energy of C_O in charge state q is defined as

$$E_f(C_O) = E_{tot}(C_O) - E_{tot}(TiO_2) - \mu_C + \mu_O + q(\varepsilon_F + E_V) + E_{cor}, \quad (1)$$

where $E_{tot}(C_O)$ is the total energy of the supercell with one C substituted for O (C_O) in a charge state q. $E_{tot}(TiO_2)$ is the total energy of the supercell without defects and ε_F is the Fermi energy ranging over the band gap. E_V is the energy of the electron at the valence band maximum (VBM), which aligns the average electrostatic potential of the atom far away from the defect site in the supercell and with the corresponding potential in a perfect crystal. The O atom that is removed from the supercell is placed in a reservoir with energy μ_O, referenced to the total energy per atom of an isolated O_2 molecule. The C atom is taken from a reservoir with energy μ_C, referenced to the total energy per atom of C in a bulk phase. Similarly, in the case of C_{Ti}, the Ti atom that is removed from the supercell is placed in a reservoir with energy μ_{Ti}, referenced to the total energy per atom of Ti in a bulk phase ($\mu_{Ti} = \tilde{\mu}_{Ti} + E_{tot}[Ti_{bulk}]$). These reference energies are given by our DFT calculations for the total energy of bulk Ti per formula unit (−9.46 eV) and half the total energy of an isolated O_2 molecule (−8.55 eV).

The final term, E_{cor}, is the image charge correction term, which corrects for the Madelung energy of the defect point charge in the uniform background. The Coulomb image-charge corrections can be written as

$$E_{cor} = \frac{\alpha_M q^2}{\varepsilon L} + \frac{2\pi q Q}{3\varepsilon L^3} \quad (2)$$

where q is the nominal charge of the defect, Q is the quadrupole moment, L is the linear size of the supercell, α_M is a Madelung constant and ε is the static dielectric constant. As recently shown by Lany and Zunger, the quadrupole term can be approximated to about one-third of the monopole term for cubic supercells.[40] For the present calculations of E_{cor}, we obtain the dielectric constant from the experimental value of 159.67.[41]

The chemical potentials $\tilde{\mu}_{Ti}$ and $\tilde{\mu}_O$ are variables but must satisfy the stability condition $\tilde{\mu}_{Ti} + \tilde{\mu}_O = \Delta H_f(TiO_2)$, where $\Delta H_f(TiO_2)$ is the formation enthalpy of TiO_2. In principle, $\tilde{\mu}_O$ can vary over a wide range from O-rich ($\tilde{\mu}_O = 0$) to O-poor ($\tilde{\mu}_O = (\Delta H_f(TiO_2) - \tilde{\mu}_{Ti})/2$). At the O-rich limit, the chemical potential of Ti is given by $\tilde{\mu}_{Ti} = \Delta H_f(TiO_2)$, while at the Ti-rich limit, $\tilde{\mu}_{Ti}$ is bound by the formation of Ti_2O_3, $2\tilde{\mu}_{Ti} + 3\tilde{\mu}_O < \Delta H_f(Ti_2O_3)$. The calculated $\Delta H_f(TiO_2)$ and $\Delta H_f(Ti_2O_3)$ using the HSE approach are −9.93 eV and −15.94 eV, which are in good agreement with the experimental values of −9.78 eV[42] and −15.74 eV,[42] respectively.

Since the Ti-to-O ratio is higher in Ti_2O_3 than in TiO_2, we expect the growth of these alternate phases to be favorable under Ti-rich growth conditions. The stable thermodynamic condition of TiO_2 is represented in the phase diagram illustrated in Fig. S1 (see ESI†). In this article, we present results of

the formation energies for O-poor and O-rich conditions. Our analysis gives the chemical potential settings $(\tilde{\mu}_{Ti}, \tilde{\mu}_O)$ corresponding to Ti-rich (O-poor) and O-rich (Ti-poor) as $(-2.10, -3.95)$ and $(-9.93, 0)$ in eV, respectively. Under the O-rich growth condition, $\tilde{\mu}_C$ is limited by the formation of the CO_2 molecule, *i.e.* $\tilde{\mu}_C = \Delta H_f(CO_2) - 2\tilde{\mu}_O$, whereas under the O-poor (Ti-rich) growth condition, $\tilde{\mu}_C$ is limited by the formation of TiC, *i.e.* $\tilde{\mu}_C = \Delta H_f(TiC) - \tilde{\mu}_{Ti}$.

The thermodynamic transition levels are given by the Fermi energy at which the formation energies of the two charged states are equal:

$$\varepsilon_D\left(q/q'\right) = \frac{E_f\left(D^q; \ \varepsilon_F = 0\right) - E_f\left(D^{q'}; \ \varepsilon_F = 0\right)}{q' - q}. \quad (3)$$

The thermodynamic transitions are represented by kinks in the plots of formation energy as a function of Fermi energy. Note that ε_F ranges over the band gap and is referenced to the VBM. Optical transitions were determined based on configuration coordinate diagrams following the standard procedure described in ref. 43.

3   Results

3.1   Fundamental properties of rutile TiO_2

Rutile TiO_2 can be described by a six-atom primitive cell with lattice parameters a and c, and an internal parameter u that defines the distance between Ti and O atoms in the plane perpendicular to the c direction, as shown in Fig. S2(a) in the ESI.† The lattice parameters calculated by HSE (using 25% HF exchange), band gap at Γ and formation enthalpy (ΔH_f) are listed in Table 1. The calculated lattice parameters are in very good agreement with the experimental values. The calculated electronic band structure and the Brillouin zone are presented in Fig. S2 (see ESI†). Our calculated band gap is 3.34 eV, slightly higher than the experimental value of 3.03 eV.[8]

3.2   Model structure of carbon doping

In principle, there are three possible ways to include C atoms in the lattice. The first one is the substitution of an O by a C atom (C_O); the second is the substitution of a Ti atom by a C atom (C_{Ti}). The third possibility is that a C atom is stabilized at an interstitial position (C_i). These three models of C impurities are shown in Fig. 1(a)–(c). We denote C_O and C_{Ti} as on-site configurations since the C atoms remain at their respective lattice sites, constrained by the crystal symmetry.

Table 1 Calculated structural parameters, band gap and formation enthalpy of rutile TiO_2

Functional	a	c/a	u/a	E_g	ΔH_f (eV)
PBE[44]	4.65	0.639	0.305	1.77	−9.33
HSE $(\alpha = 0.20)$[44]	4.59	0.642	0.305	3.05	−9.73
This work $(\alpha = 0.25)$	4.59	0.644	0.305	3.34	−9.93
Expt.[8,42,45]	4.59	0.644	0.306	3.03	−9.78
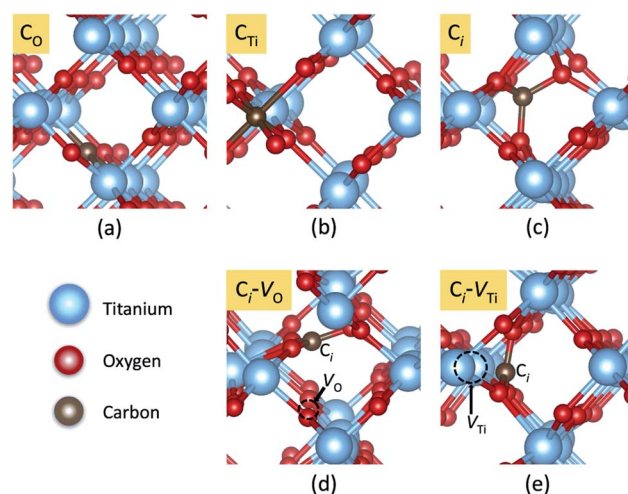
Fig. 1 Local atomic structures of carbon impurities: (a) C_O, (b) C_{Ti}, (c) C_i, (d) C_i–V_O and (e) C_i–V_{Ti} in rutile TiO_2. The red, blue, and brown spheres represent O, Ti, and C atoms, respectively.

However, in the case of C_O and C_{Ti}, the carbon atoms can significantly shift from the ideal lattice positions toward three nearby O atoms, stabilizing the low-symmetry (off-site) configurations. For C_O, the off-site configuration can be represented as a complex between interstitial C and an oxygen vacancy (C_i–V_O), while for C_{Ti}, the off-site configuration can be represented as interstitial C and a nearby titanium vacancy (C_i–V_{Ti}). The most energetically favorable low-symmetry (off-site) configurations of C_O and C_{Ti} are shown in Fig. 1(d) and (e), respectively.

3.3   Carbon doped TiO_2: formation energies

In our calculations, we vary the charge states of the defects to identify the most stable charge state. The formation energies of C_O, C_{Ti}, C_i, C_i–V_O and C_i–V_{Ti} as a function of the Fermi level are shown in Fig. 2. The vertical dashed line indicates the experimental band gap of 3.03 eV.[8] Only the formation energy
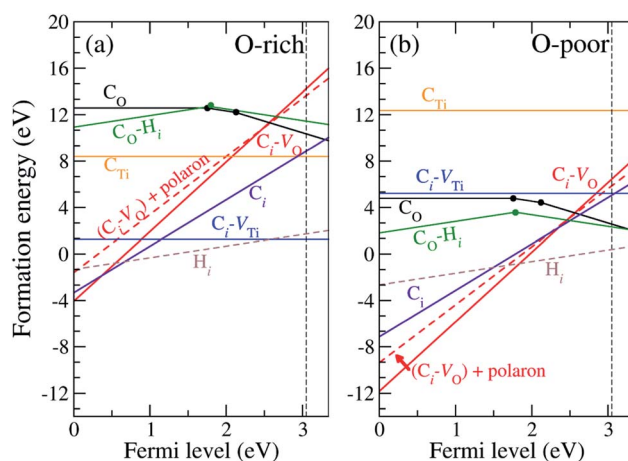

Fig. 2 Defect formation energies as a function of Fermi energy under (a) O-rich and (b) O-poor conditions. The vertical dashed line indicates the experimental band gap.[8]

associated with the lowest-energy charge state of each defect is shown for the corresponding Fermi-level position.

Since C has two fewer electrons than O, C_O is likely to be negatively charged and acts as an acceptor. Fig. 2 shows that C_O is stable in the neutral, − and 2− charge states with thermodynamic transition levels $\varepsilon(0/-)$ and $\varepsilon(-/2-)$ located at 1.77 and 2.12 eV above the VBM, indicating that C_O is a deep acceptor with positive-U behavior. We find that C_O is the prevalent defect under the O-poor limit for Fermi-level positions near the conduction band minimum (CBM). Deep transition levels of C_O indicate that it induces impurity states in the band gap, which likely gives rise to optical transitions with lower energy than the band gap. The calculated density of states for C_O is illustrated in Fig. S3 (see ESI†).

For C_i, we find that the C atom binds to four O atoms with an average C–O bond length of 1.40 Å. Since O has a much higher electronegativity than C, the C atom tends to donate its four valence electrons to the surrounding O atoms. Thus C_i is exclusively stable in the 4+ charge state, acting as a quadruple donor. Since the oxygen vacancy, V_O, in rutile TiO₂ is stable in the 2+ charge state[44] and C_i is stable in the 4+ charge state, the C_i–V_O complex is reasonably expected to occur in the 6+ charge state. Our calculations show that the C_i–V_O complex is stable in the 6+ charge state and is prevalent under O-poor growth conditions for Fermi-level positions from 0 to 2.46 eV above the VBM. In addition, this complex can trap an additional electron in the form of a small polaron. The formation energy of (C_i–V_O) + 1 polaron is included in Fig. 2, indicating that it becomes more stable than (C_i–V_O) for Fermi-level positions higher than 2.46 eV. In C_i–V_O, the C atom binds with three neighboring oxygen atoms, forming a carbonate ion-like structure, CO_3^{2-}, as shown in Fig. 1(d). The average planar C–O bond length is 1.28 Å, which is very close to the calculated C–O bond length in CaCO₃ of 1.29 Å.

Since Ti and C are isovalent, the substitution of Ti by a C atom does not create an extra electron or hole and is expected to occur in the neutral charge state. Our calculations show that C_{Ti} does not create defect levels in the band gap and thus is stable in the neutral charge state for the whole range of Fermi levels. We also find that a C atom is likely to be displaced from the Ti site and bind with three nearby O atoms in the form of a C_i–V_{Ti} complex (see Fig. 1(e)), which is 6 eV lower in energy than C_{Ti}. The average planar and apical C–O bond lengths of C_{Ti} are 1.55 Å and 2.10 Å, respectively. In C_i–V_{Ti}, the interstitial carbon atom also binds with three neighboring oxygen atoms, forming a carbonate ion-like structure, CO_3^{2-}, as shown in Fig. 1(e), with an average C–O bond length of 1.29 Å. Much shorter C–O bond lengths in C_i–V_{Ti} compared to those in C_{Ti} reflect much stronger C–O bonds, resulting in a significantly lower formation energy. Under the O-rich limit, the C_i–V_{Ti} complex is a predominant defect for Fermi-level values higher than 1.13 eV above the VBM. When the Fermi level decreases toward the VBM, the donor-type defects C_i and (C_i–V_O) become more stable. However, it is unlikely for TiO₂ to have that relatively low Fermi level.

In addition, we consider the effects of hydrogen, which is ubiquitous and could be unintentionally incorporated during the growth process. Hydrogen has been reported to play an

important role in the electrical properties of many oxides and affects the optical absorption of N impurities in TiO₂[33] and SrTiO₃.[46] First, interstitial H (H_i) is found to prefer to bind with a host O atom without introducing any state in the band gap. Our calculations show that H_i is stable in the 1+ charge state, acting as a shallow donor. In addition, we find that an extra electron can be trapped at a Ti site in association with the presence of H_i^+. This result is in agreement with the DFT+U calculations.[47] However, we do not consider this electron trapping here because the calculations could be very complicated and beyond the scope of the present work. Besides, the migration barrier of H_i^+ in TiO₂ has been reported to be 0.59 eV parallel and 1.28 eV perpendicular to the tetragonal c-axis,[48] indicating that it is highly mobile at low temperature unless it is trapped by other defects or impurities. H_i^+ can be trapped by C_O acceptors *via* coulombic attraction.

Our calculated formation energies show that the C_O–H_i complex is stable in + and − charge states with the transition level $\varepsilon(+/-)$ located at 1.78 eV above the VBM. This characteristic of the complex is unlike N_O–H_i in TiO₂,[33] which is stable only in the neutral charge state. For N_O^- in TiO₂, the in-gap localized states of N_O^- are completely passivated by H_i. For C_O^{2-}, H_i partially passivates one of the localized in-gap states, leaving the other C-related states in the band gap. The average C–H bond length in the C_O–H_i complex is 1.096 Å, which is very close to the calculated C–H bond length in the CH₄ molecule of 1.09 Å. The local atomic geometries of H_i and C_O–H_i are illustrated in Fig. 3.

We also calculated the binding energy of the C_O–H_i complex, defined as

$$E_b[(C_O\text{–}H_i)^q] = E_f[C_O{}^q] + E_f[H_i^+] - E_f[(C_O\text{–}H_i)^q], \qquad (4)$$

where $E_f[(C_O\text{–}H_i)^q]$ is the formation energy of the complex in charge state q ($q = +, -$). $E_f[H_i^+]$ is the formation energy of H_i in the 1+ charge state, and $E_f[C_O{}^q]$ is the formation energy of C_O in charge state q' ($q' = 0, -, 2-$). The calculated binding energy of the C_O–H_i complex is determined as a function of the Fermi level, as shown in Fig. 4. For Fermi-level values near the CBM, the binding energy is 0.61 eV, which is comparable to that of N_O–H_i in rutile TiO₂ (0.58 eV).[33] However, the binding energy is reduced to 0.31 eV when the Fermi level moves forward to the valence band. We note that the binding energies remain the
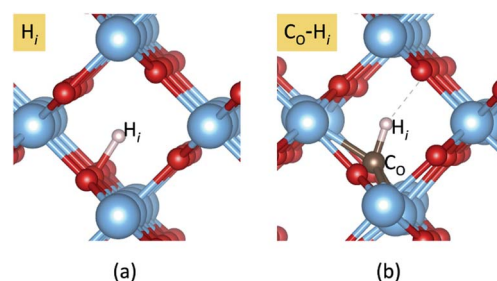

Fig. 3 Local atomic structures of (a) H_i and (b) C_O−H_i in rutile TiO₂. The red and blue spheres represent O and Ti atoms, respectively. The brown and pink spheres represent the carbon and hydrogen impurities.
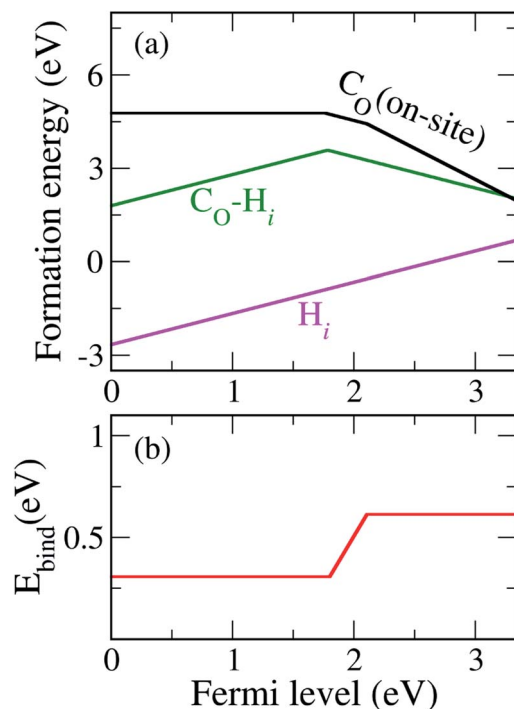
Fig. 4 (a) Formation energies of C_O, H_i, and the C_O–H_i complex under the O-poor limit. (b) The calculated binding energy (E_{bind}) of the C_O–H_i complex as a function of the Fermi level.

Fig. 5 Configuration coordinate diagram for C_O in rutile TiO$_2$. The formation energies correspond to the similar O-poor condition in Fig. 2 and ε_F at (a) CBM for the $C_O^{2-} + h\nu \rightarrow C_O^- + e^-$ process and at (b) VBM for the $C_O^- + h\nu \rightarrow C_O^{2-} + h^+$ process.

same regardless of O chemical potentials. We can also address the stability of the complex by estimating the dissociation energy given by $E_b[C_O–H_i]^- + E_m(H_i^+)$, where $E_m(H_i^+)$ is the calculated migration barrier of interstitial H of 0.58 eV.[47] The dissociation energy is estimated as 1.2 eV, thus indicating that $(C_O–H_i)^-$ can be stable at temperatures up to ∼187 °C. Our analysis shows that in the presence of hydrogen, $(C_O–H_i)^-$ will be formed and predominant in n-type TiO$_2$ under the O-poor limit.

3.4 Optical absorption and emission

Here we focus on C_O and C_O–H_i, which introduce deep levels in the band gap and could give rise to optical transitions with lower energy than the band gap of TiO$_2$. The optical properties of C_O were determined through the configuration coordinate diagram shown in Fig. 5. The optical transition associated with C_O occurs through the process $C_O^{2-} + h\nu \rightarrow C_O^- + e^-$, as represented in Fig. 5(a). C_O^{2-} absorbs a photon and is converted to C_O^- with an electron in the conduction band. The absorption energy was obtained by calculating the difference in the formation energy between C_O^- in the C_O^{2-} lattice geometry and C_O^{2-}. The calculated absorption energy corresponds to the C_O-related absorption peak centered at 1.83 eV, in which an electron is excited from the fully occupied state of C_O^{2-} to the conduction band. The calculated emission energy, representing the recombination of the electron in the conduction band with the hole in C_O^-, i.e. $C_O^- + e^- \rightarrow C_O^{2-} + h\nu$, is 0.74 eV.

Besides, another optical transition of C_O occurs through the process $C_O^- + h\nu \rightarrow C_O^0 + e^-$, in which C_O^- absorbs a photon,
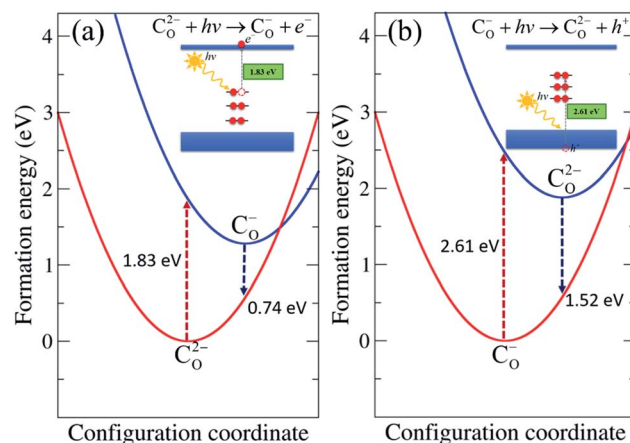
converting it to C_O^0 with an electron in the conduction band. The absorption energy was obtained by calculating the difference in the formation energy between C_O^- and C_O^0 in the C_O^- lattice geometry. The calculated absorption energy for this process is 2.18 eV. The calculated emission energy for $C_O^0 + e^- \rightarrow C_O^- + h\nu$ is 0.34 eV.

We also considered the transition through the process $C_O^- + h\nu \rightarrow C_O^{2-} + h^+$, as depicted in Fig. 5(b), in which an electron is transferred to C_O^-, converting it into C_O^{2-} with a hole in the valence band. The analogous transition process $C_O^0 + h\nu \rightarrow C_O^- + h^+$ also takes place. The absorption energies of both processes were calculated by constructing the configuration coordinate diagram, yielding values of 2.61 eV and 3.01 eV, respectively. The absorption energies associated with valence band electron exchange were slightly higher than those associated with conduction band electron exchange. The emission energies are 1.52 eV for $C_O^{2-} + h^+ \rightarrow C_O^- + h\nu$ and 1.17 eV for $C_O^- + h^+ \rightarrow C_O^0 + h\nu$.

In addition, we consider the optical transition associated with $(C_O–H_i)$ through the process $(C_O–H_i)^- + h\nu \rightarrow (C_O–H_i)^0 + e^-$, in which an electron is excited from $(C_O–H_i)^-$ to the conduction band, yielding an absorption energy of 2.16 eV. Another transition process, $(C_O–H_i)^0 + h\nu \rightarrow (C_O–H_i)^- + h^+$, gives an absorption energy of 2.40 eV. These absorption energies are slightly higher than the absorption energy associated with C_O. All the plausible optical transition processes and absorption and emission energies associated with C_O and the $(C_O–H_i)$ complex are listed in Table 2.

Our calculated optical absorption energies listed in Table 2 elucidate that both C_O and the $(C_O–H_i)$ complex give rise to optical absorption in the visible-light region. Most of the emission energies associated with C_O and the $(C_O–H_i)$ complex are in the infrared region. These C-related impurities become predominant in n-type rutile TiO$_2$ under highly O-deficient conditions. In experiments, C-doped TiO$_2$ samples often exhibit mixed-phase structures (anatase–rutile, anatase–brookite or anatase–rutile–brookite).[49–52] An effort to prepare C-

Table 2 The optical transition processes and absorption and emission energies associated with C_O and the (C_O–H_i) complex. The predicted colors corresponding to the absorption and emission energies are also listed

Procedure	Type	eV	Color
$C_O^{2-} + h\nu \rightarrow C_O^- + e^-$	Absorption, CBM	1.83	Red
$C_O^- + h\nu \rightarrow C_O^0 + e^-$	Absorption, CBM	2.18	Yellow
$C_O^- + e^- \rightarrow C_O^{2-} + h\nu$	Emission, CBM	0.74	IR
$C_O^0 + e^- \rightarrow C_O^- + h\nu$	Emission, CBM	0.34	IR
$C_O^- + h\nu \rightarrow C_O^{2-} + h^+$	Absorption, VBM	2.61	Blue
$C_O^0 + h\nu \rightarrow C_O^- + h^+$	Absorption, VBM	3.01	Violet
$C_O^{2-} + h^+ \rightarrow C_O^- + h\nu$	Emission, VBM	1.52	IR
$C_O^- + h^+ \rightarrow C_O^0 + h\nu$	Emission, VBM	1.17	IR
$(C_O–H_i)^- + h\nu \rightarrow (C_O–H_i)^0 + e^-$	Absorption, CBM	2.16	Yellow
$(C_O–H_i)^0 + h\nu \rightarrow (C_O–H_i)^+ + e^-$	Absorption, CBM	1.60	Red
$(C_O–H_i)^+ + e^- \rightarrow (C_O–H_i)^0 + h\nu$	Emission, CBM	1.41	IR
$(C_O–H_i)^0 + e^- \rightarrow (C_O–H_i)^- + h\nu$	Emission, CBM	0.94	IR
$(C_O–H_i)^+ + h\nu \rightarrow (C_O–H_i)^0 + h^+$	Absorption, VBM	1.94	Red
$(C_O–H_i)^0 + h\nu \rightarrow (C_O–H_i)^- + h^+$	Absorption, VBM	2.40	Green
$(C_O–H_i)^- + h^+ \rightarrow (C_O–H_i)^0 + h\nu$	Emission, VBM	1.17	IR
$(C_O–H_i)^0 + h^+ \rightarrow (C_O–H_i)^+ + h\nu$	Emission, VBM	1.74	Red

doped rutile TiO_2 has also been reported; however, C dopants were not successfully incorporated into the lattice sites.[53] Pure C-doped rutile TiO_2 samples are still very scarce. Recently, black carbon-doped rutile TiO_2 was reported to have been successfully synthesized by the substitution of O at C sites in TiC film.[54] However, it is ambiguous whether C atoms were atomically dispersed in the TiO_2 lattice sites, as indicated by the dominant C–C bond characteristics in the X-ray photoemission spectroscopy peaks. Therefore, we do not directly compare our calculated optical absorption energies with the available experimental values. Our results presented here are provided to support future experimental identification of C impurities using optical-transition measurement techniques.

4 Conclusions

In summary, we employed hybrid density-functional calculations to investigate the thermodynamic stability and the effects of C impurities on optical absorption in rutile TiO_2. We find that, among other C impurities, only substitutional C_O introduces defect levels in the band gap and gives rise to optical absorption in the visible region. Our calculated formation energies show that C_O is a deep donor and energetically stable in n-type TiO_2 under the O-poor limit. When the oxygen partial pressure increases, C_i–V_{Ti} becomes energetically stable in n-type TiO_2; however, it is electrically and optically inactive. We also find that hydrogen can bind with C_O in a (C_O–H_i) complex which is stable up to relatively high temperature. This complex does not completely passivate the visible-light absorption induced by C_O but leads to a net red-shift in the absorption edge.

In addition, we find that C_i and C_i–V_O are shallow donors and can act as compensating centers for C_O acceptor and p-type dopants in rutile TiO_2. Therefore, substrates, precursors or growth processes containing carbon should be avoided for the efficient fabrication of p-type rutile TiO_2. Our results presented

in this work reveal the true nature of C impurities and the C impurity–H complex in rutile TiO_2. They not only serve as a guide for C impurity identification in rutile TiO_2 but also pave the way for new applications of TiO_2 in optoelectronics and photovoltaics.

Conflicts of interest

There are no conflicts to declare.

Acknowledgements

Notes and references

1 M. Ni, M. K. Leung, D. Y. Leung and K. Sumathy, *Renewable Sustainable Energy Rev.*, 2007, **11**, 401–425.
2 L. Hao, J. Wang, F.-Q. Bai, M. Xie and H.-X. Zhang, *Eur. J. Inorg. Chem.*, 2015, **2015**, 5563–5570.
3 T.-F. Lu, W. Li, F.-Q. Bai, R. Jia, J. Chen and H.-X. Zhang, *J. Mater. Chem. A*, 2017, **5**, 15567–15577.
4 L. Liu, H. Zhao, J. M. Andino and Y. Li, *ACS Catal.*, 2012, **2**, 1817–1828.
5 T. Ohno, K. Sarukawa and M. Matsumura, *New J. Chem.*, 2002, **26**, 1167–1170.
6 S. Mahshid, M. Askari, M. S. Ghamsari, N. Afshar and S. Lahuti, *J. Alloys Compd.*, 2009, **478**, 586–589.
7 D. A. Hanaor, I. Chironi, I. Karatchevtseva, G. Triani and C. C. Sorrell, *Adv. Appl. Ceram.*, 2012, **111**, 149–158.
8 A. Amtout and R. Leonelli, *Phys. Rev. B: Condens. Matter Mater. Phys.*, 1995, **51**, 6842.
9 V. E. Henrich and R. L. Kurtz, *Phys. Rev. B: Condens. Matter Mater. Phys.*, 1981, **23**, 6280–6287.
10 D. Duonghong, E. Borgarello and M. Graetzel, *J. Am. Chem. Soc.*, 1981, **103**, 4685–4690.
11 E. Bae, W. Choi, J. Park, H. S. Shin, S. B. Kim and J. S. Lee, *J. Phys. Chem. B*, 2004, **108**, 14093–14101.
12 H. Kisch, L. Zang, C. Lange, W. F. Maier, C. Antonius and D. Meissner, *Angew. Chem., Int. Ed.*, 1998, **37**, 3034–3036.
13 C.-y. Wang, D. W. Bahnemann and J. K. Dohrmann, *Chem. Commun.*, 2000, 1539–1540.
14 H. Yamashita, M. Honda, M. Harada, Y. Ichihashi, M. Anpo, T. Hirao, N. Itoh and N. Iwamoto, *J. Phys. Chem. B*, 1998, **102**, 10707–10711.
15 R. Asahi, T. Morikawa, T. Ohwaki, K. Aoki and Y. Taga, *Science*, 2001, **293**, 269–271.
16 Y. Park, W. Kim, H. Park, T. Tachikawa, T. Majima and W. Choi, *Appl. Catal., B*, 2009, **91**, 355–361.

17 S. Livraghi, M. C. Paganini, E. Giamello, A. Selloni, C. Di Valentin and G. Pacchioni, *J. Am. Chem. Soc.*, 2006, **128**, 15666–15671.

18 S. U. Khan, M. Al-Shahry and W. B. Ingler, *Science*, 2002, **297**, 2243–2245.

19 Y. Choi, T. Umebayashi and M. Yoshikawa, *J. Mater. Sci.*, 2004, **39**, 1837–1839.

20 H. Irie, Y. Watanabe and K. Hashimoto, *Chem. Lett.*, 2003, **32**, 772–773.

21 S.-W. Hsu, T.-S. Yang, T.-K. Chen and M.-S. Wong, *Thin Solid Films*, 2007, **515**, 3521–3526.

22 Y. Li, D.-S. Hwang, N. H. Lee and S.-J. Kim, *Chem. Phys. Lett.*, 2005, **404**, 25–29.

23 W. Ren, Z. Ai, F. Jia, L. Zhang, X. Fan and Z. Zou, *Appl. Catal., B*, 2007, **69**, 138–144.

24 T. Ohno, T. Tsubota, K. Nishijima and Z. Miyamoto, *Chem. Lett.*, 2004, **33**, 750–751.

25 S. Sakthivel and H. Kisch, *Angew. Chem., Int. Ed.*, 2003, **42**, 4908–4911.

26 R. Klaysri, M. Ratova, P. Praserthdam and P. J. Kelly, *Nanomaterials*, 2017, **7**, 113.

27 C. Di Valentin, G. Pacchioni and A. Selloni, *Chem. Mater.*, 2005, **17**, 6656–6665.

28 J. P. Perdew, K. Burke and M. Ernzerhof, *Phys. Rev. Lett.*, 1996, **77**, 3865–3868.

29 P. Mori-Sánchez, A. J. Cohen and W. Yang, *J. Chem. Phys.*, 2006, **125**, 201102.

30 V. Polo, E. Kraka and D. Cremer, *Mol. Phys.*, 2002, **100**, 1771–1790.

31 B. G. Janesko, T. M. Henderson and G. E. Scuseria, *Phys. Chem. Chem. Phys.*, 2009, **11**, 443–454.

32 C. Freysoldt, B. Grabowski, T. Hickel, J. Neugebauer, G. Kresse, A. Janotti and C. G. Van de Walle, *Rev. Mod. Phys.*, 2014, **86**, 253.

33 J. Varley, A. Janotti and C. Van de Walle, *Adv. Mater.*, 2011, **23**, 2343–2347.

34 J. Heyd, G. E. Scuseria and M. Ernzerhof, *J. Chem. Phys.*, 2003, **118**, 8207.

35 P. E. Blöchl, *Phys. Rev. B: Condens. Matter Mater. Phys.*, 1994, **50**, 17953–17979.

36 G. Kresse and J. Furthmüller, *Comput. Mater. Sci.*, 1996, **6**, 15–50.

37 S. Lany and A. Zunger, *Phys. Rev. B: Condens. Matter Mater. Phys.*, 2009, **80**, 085202.

38 P. Deák, B. Aradi and T. Frauenheim, *Phys. Rev. B: Condens. Matter Mater. Phys.*, 2011, **83**, 155207.

39 J. Paier, M. Marsman, K. Hummer, G. Kresse, I. C. Gerber and J. G. Ángyán, *J. Chem. Phys.*, 2006, **124**, 154709.

40 S. Lany and A. Zunger, *Phys. Rev. B: Condens. Matter Mater. Phys.*, 2008, **78**, 235104.

41 R. A. Parker, *Phys. Rev.*, 1961, **124**, 1719.

42 G. L. Humphrey, *J. Am. Chem. Soc.*, 1951, **73**, 1587–1590.

43 C. G. Van de Walle and J. Neugebauer, *J. Appl. Phys.*, 2004, **95**, 3851–3879.

44 A. Janotti, J. Varley, P. Rinke, N. Umezawa, G. Kresse and C. Van de Walle, *Phys. Rev. B: Condens. Matter Mater. Phys.*, 2010, **81**, 085212.

45 F. A. Grant, *Rev. Mod. Phys.*, 1959, **31**, 646–674.

46 P. Reunchan, N. Umezawa, A. Janotti, T. Jiraroj, S. Limpijumnong, *et al.*, *Phys. Rev. B*, 2017, **95**, 205204.

47 F. Filippone, G. Mattioli, P. Alippi and A. A. Bonapasta, *Phys. Rev. B: Condens. Matter Mater. Phys.*, 2009, **80**, 245203.

48 J. B. Bates, J. Wang and R. Perkins, *Phys. Rev. B: Condens. Matter Mater. Phys.*, 1979, **19**, 4130.

49 M. Ratova, R. Klaysri, P. Praserthdam and P. J. Kelly, *Vacuum*, 2018, **149**, 214–224.

50 Y.-T. Lin, C.-H. Weng, Y.-H. Lin, C.-C. Shiesh and F.-Y. Chen, *Sep. Purif. Technol.*, 2013, **116**, 114–123.

51 J. Jia, D. Li, J. Wan and X. Yu, *J. Ind. Eng. Chem.*, 2016, **33**, 162–169.

52 A. Bai, W. Liang, G. Zheng and J. Xue, *J. Wuhan Univ. Technol., Mater. Sci. Ed.*, 2010, **25**, 738–742.

53 E. M. Neville, J. Ziegler, J. D. MacElroy, K. R. Thampi and J. A. Sullivan, *Appl. Catal., A*, 2014, **470**, 434–441.

54 S. Guan, L. Hao, H. Yoshida, Y. Lu and X. Zhao, *Mater. Express*, 2017, **7**, 509–515.